

**Extreme events in a broad-area semiconductor laser with coherent injection**Cristina Rimoldi,<sup>1</sup> Mansour Eslami<sup>2</sup>,, Franco Prati,<sup>3</sup> and Giovanna Tissoni<sup>4,\*</sup><sup>1</sup>*Dipartimento di Elettronica e Telecomunicazioni, Politecnico di Torino, Corso Duca degli Abruzzi 24, IT-10129 Torino, Italy*<sup>2</sup>*Department of Physics, University of Guilan, P.O. Box 41335-1914, Rasht, Iran*<sup>3</sup>*Dipartimento di Scienza e Alta Tecnologia, Università dell'Insubria, Via Valleggio 11, IT-22100 Como, Italy*<sup>4</sup>*Université Côte d'Azur, CNRS, Institut de Physique de Nice, 1361 Route des Lucioles, FR-06560 Valbonne, France*

(Received 23 July 2021; accepted 19 January 2022; published 25 February 2022)

Spatiotemporal extreme events are interesting phenomena, both from a fundamental point of view, as manifestations of complexity in dynamical systems, and for their possible applications in different research fields. Here, we present some recent results for extreme events in spatially extended semiconductor laser systems (broad-area vertical cavity surface-emitting lasers) with coherent injection. We study the statistics of spatiotemporal intensity peaks occurring in the transverse  $(x, y)$  section of the field perpendicular to the light propagation direction and identify regions in the parameter space where extreme events are more likely to occur. Searching for precursors of these phenomena, we concentrate, on the one hand, on the spatiotemporal dynamics of the field phase and, in particular, on the presence of optical vortices in the vicinity of an extreme event. On the other hand, we focus on the laser gain dynamics and the phase-space trajectories of the system close to the occurrence of an extreme event. Both these complementary approaches are successful and allow us to shed some light on potential prediction strategies.

DOI: [10.1103/PhysRevA.105.023525](https://doi.org/10.1103/PhysRevA.105.023525)**I. INTRODUCTION**

In the last few decades, extreme events have been studied in many different physical systems, from hydrodynamics to optics. In the latter field, they have been defined as optical rogue waves (RWs) [1] and were the topic of a vast amount of literature in many different optical systems (for a review, see Refs. [2–4] and references therein). Optical fibers and fiber lasers have been identified since the beginning as systems of choice for optical rogue-wave studies due to their natural longitudinal extension (see, for instance, Refs. [5–7] for conservative cases and Refs. [8,9] for dissipative rogue waves in resonators and laser devices).

Semiconductor systems have also emerged as experimentally convenient test beds for the analysis of extreme phenomena. For instance, low-dimensional semiconductor systems, in which the wave envelope is severely constrained by boundary conditions, served to demonstrate that the emergence of rogue events can be associated with an external crisis in a chaotic regime [10], thus showing the deterministic character of these extreme events. This deterministic nature was also revealed in the analysis of delayed-feedback semiconductor lasers in which the effect of increased noise reduces the probability of rogue waves by preventing the dynamics from approaching the narrow path in the phase space that leads to extreme pulses [11].

Various mechanisms have been identified for the formation of rogue waves, from modulational instability [12] to soliton and breather occurrence [5] and competition of extended

structures associated with opposite signs of nonlinearity [13,14]. Rogue waves have also been reported from the interaction of optical vortices with opposite chiral charges [15]. However, a unifying mechanism for extreme-event generation in the optical context and thus their potential prediction [16,17] remains undiscovered.

Very recently, extreme events were studied both experimentally and numerically [18,19] in the intensity of the electric field emitted by a monolithic broad-area vertical cavity surface-emitting laser (VCSEL) with a saturable absorber for the case of a linear pump (which reduces the number of transverse dimensions to one), and spatiotemporal chaos was claimed to be at the dynamical origin of these objects. The very same system has been under investigation in a two-dimensional configuration, where spatiotemporal extreme events have been identified as maxima of the field intensity in the three-dimensional space  $(x, y, t)$  [20] and can be controlled through harmonic pump modulation [21]. Extreme events have been analyzed following their various definitions and through different RW indicators, and the best parameter choice to observe them has been identified. Furthermore, it has been possible to determine the typical temporal and spatial size (FWHM) expected for such extreme events and to compare it with stationary and oscillating solitons. As suggested in Ref. [22] for a similar system, we believe that two-dimensional spatial effects play a crucial role in the formation of extreme events.

Spatially extended semiconductor lasers in a macroscopic ring-cavity configuration and with coherent injection have also been extensively studied in recent years [23,24], and extreme events have been identified in different parametric regimes. Interestingly, the dynamics of the electric-field phase

\*giovanna.tissoni@inphyni.cnrs.fr

seems to play an important role in the generation of extreme events, allowing us to draw a natural analogy with the particular kind of dissipative solitons existing in these systems, i.e., phase solitons [25], with which extreme events share their chiral nature.

In this paper we consider a broad-area semiconductor laser (VCSEL) with coherent injection [26] and focus on the (spatiotemporal) “turbulent” regime occurring for low values of injection where the lower branch of the homogeneous stationary solution (HSS) is Hopf unstable. A similar regime was studied in [15] for a generic class-A laser when the atomic medium and injection are at resonance with each other, i.e., with  $\Delta = 0$ , and was characterized as vortex turbulence. We would like to stress that, even if the model here preserves some of the features illustrated in [15] (for instance, we will see that the phase of the electric field still seems to play an important role), the system dynamics is dramatically different. This is because (i) the insertion of the linewidth enhancement factor  $\alpha$  for semiconductor lasers in the model equations, playing the role of the atomic detuning  $\Delta$ , changes the degree of complexity of the observed turbulence and (ii) the carrier density dynamics is not fast enough to be (adiabatically or nonadiabatically) eliminated, which leads to interesting consequences in the prediction of extreme events.

Finally, some dynamical similarities can be drawn with the model studied in [23,24], for a semiconductor ring laser with injection. As mentioned already in [27], for a model fairly similar to the one utilized here, the exponential decay of the merging time of two cavity solitons (CSs) as a function of their initial distance somehow resembles the transition time necessary for two phase solitons carrying a single chiral charge along the propagation direction to merge in a phase soliton complex carrying a double charge. The main difference between these two cases consists of the fact that in [23,24] the system (single) spatial dimension was given by the propagation along the ring cavity, while here the two spatial dimensions describe the laser transverse plane and are perpendicular to the propagation direction.

This paper is structured as follows. In Sec. II, we illustrate the theoretical model and show the main results of a linear stability analysis of the homogeneous steady-state solution. In Sec. III, we show the results of numerical simulations and statistically prove the presence of extreme events in the system and study the mechanism leading to their generation, with a particular focus on optical vortices. In Sec. IV, we study rogue-wave occurrence in terms of optical-gain dynamics, and in Sec. V, we prove that these events persist in the presence of a finite-pump profile. Finally, in Secs. VI and VII, we discuss our work, draw our conclusions, and suggest some possible extensions of these results.

## II. THEORY

The model describing a broad-area semiconductor laser (VCSEL) with injection is given by the following set of rate equations:

$$\begin{aligned} \dot{E} &= \sigma[E_I - (1 + i\theta)E + (1 - i\alpha)DE + (d + i)\nabla_{\perp}^2 E], \\ \dot{D} &= \mu - D(1 + |E|^2), \end{aligned} \quad (1)$$

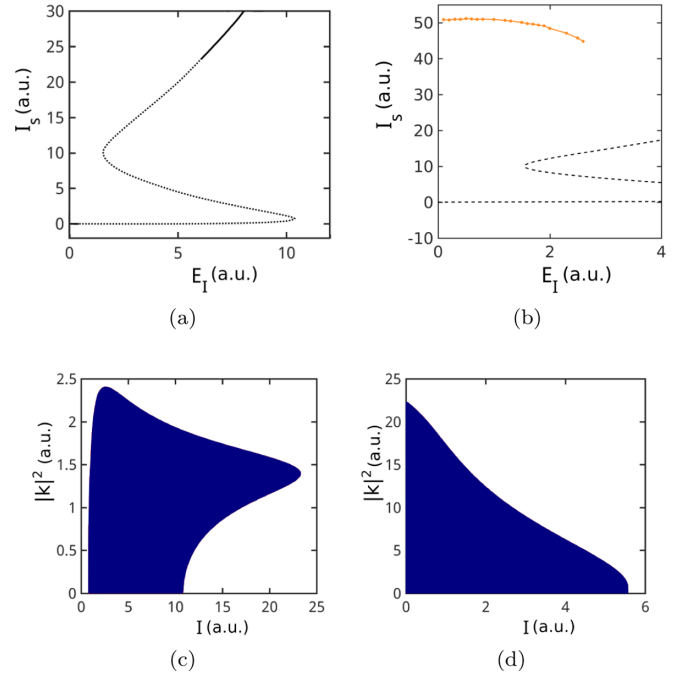


FIG. 1. (a) Homogeneous stationary solution (HSS) for the laser intensity  $I_s = |E_s|^2$  as a function of  $E_I$ . (b) The same HSS plotted together with the branch for the stable turbulent solution (orange line with dots). (c) Stationary and (d) Hopf instability domains for the fixed parameters  $\alpha = 4$ ,  $\theta = -2$ ,  $\mu = 6$ ,  $d = 0.01$ , and  $\sigma = 400$ .

which derives from a set of effective Maxwell-Bloch equations known for properly describing this kind of system [26], where the polarization of the semiconductor medium has been adiabatically eliminated. The dynamical variables  $E$  and  $D$  are, respectively, the slowly varying electric field and the semiconductor carrier density.  $E_I$  is the injected field amplitude,  $\theta$  represents the detuning between the cavity and the injected field frequencies,  $\alpha$  is the linewidth enhancement factor typical of semiconductor lasers,  $\sigma$  is the ratio of the carrier lifetime to photon lifetime, and  $\mu$  is the injection current (the free-running laser threshold is  $\mu_{\text{thr}} = 1$ ). For  $\theta + \alpha = 0$  the injected field is resonant with the free-running laser frequency. Finally,  $d$  is a diffusive term phenomenologically introduced to take into account a finite linewidth for the laser gain. A detailed analytic derivation for this term from a nonstandard adiabatic elimination of the polarization can be found in [28] for a broad-area laser with a saturable absorber. Time is scaled to the carrier lifetime ( $\approx 1$  ns), and space is scaled to the square root of the diffraction parameter (leading to a space unit of about  $4 \mu\text{m}$ ).

The HSS for the model in Eq. (1) reads  $E_s = |E_s| \exp(i\phi_s)$  and  $D_s = \mu / (1 + |E_s|^2)$ , with

$$E_I^2 = |E_s|^2 [(1 - D_s)^2 + (\theta + \alpha D_s)^2], \quad (2)$$

$$\phi = \arctan \left( \frac{\theta + \alpha D_s}{D_s - 1} \right). \quad (3)$$

In Fig. 1(a) we plot Eq. (2) for the laser intensity as a function of the injection amplitude for the following choice of parameters:  $\alpha = 4$ ,  $\theta = -2$ ,  $\mu = 6$ , and  $\sigma = 400$ . In particular, the given value of  $\sigma$  implies the values  $\tau_p = 2.5$  ps for the photon

lifetime and  $\tau_c = 1$  ns for the carrier recombination time, according to the literature and experimental measurements [26]. The diffusion term  $d = 0.01$  was chosen as the smallest possible value to avoid self-collapsing. In Figs. 1(c) and 1(d) we illustrate, respectively, the stationary and Hopf instability domains in the plane defined by the square modulus of the transverse wave vector  $|k|^2 = k_x^2 + k_y^2$  and the laser intensity. According to Figs. 1(c) and 1(d) the HSS is stationary unstable in the negative-slope branch (plane-wave instability,  $|k| = 0$ ) and in part of the upper branch (modulational or Turing instability, with  $|k| \neq 0$ ) and Hopf unstable in the lower branch.

For a slightly different model and a lower current value that is still above the free-running laser threshold, the interaction of cavity solitons was recently investigated in the presence of a lower HSS branch that was only partially Hopf unstable and compared with similar results for a soliton merging time in hydrophobic materials [27]. Here, we focus instead on the model dynamics when the system undergoes Hopf instability in its entire lower branch (i.e., for low values of injection). We would also like to point out that, different from [20], in which parameter regions with the coexistence of CSs and spatiotemporal chaos could be found, in the present context CSs exist only where (part of) the lower HSS branch is stable, as in [27], given the requirement for a stable background.

Although stable CSs have been reported to exist atop temporally (due to Hopf instability) [26,29] and/or spatially (due to Turing instability) [30] unstable backgrounds, in the present model a profile comparison with CSs is not possible since extreme events are found for values of the current for which the coexistence of a higher-intensity spatially modulated branch and a homogeneous low-intensity branch, which is essential to the creation of CSs, is absent. For the choice of parameter values indicated above, the system exhibits a turbulent behavior in the branch highlighted by the orange line with dots in Fig. 1(b) for  $0 < E_I < 2.6$ , where we illustrate the temporal average of the spatial maxima recorded in the transverse plane during 25-ns-long simulations. In Fig. 1(b), a decrease in the value of averaged maxima for higher values of injection is evident.

### III. EXTREME EVENTS AND THEIR STATISTICS

In order to characterize the presence of extreme events in the system, we ran simulations for the set of parameters mentioned in the previous section, fixed  $\mu = 6$ , and varied the injection amplitude  $E_I$  (and, vice versa, fixed  $E_I = 0.5$  and varied  $\mu$ ). For each simulation we initialized the system long enough to overcome any transient behavior and then performed data acquisition for a 25-ns-long window (unless stated otherwise). The sampling rate in the transverse plane was 1 ps on a grid size of  $256 \times 256$  pixels (corresponding approximately to  $256 \times 256 \mu\text{m}^2$  when a space step of 0.25 is adopted, as in most of our simulations).

An estimation of the data extremeness can be obtained by computing the probability density function (PDF) of all the values explored by the electric-field intensity  $I$  during the simulations. As discussed in the literature [2], if the ‘‘surface elevation’’ of the real and imaginary parts of the electric field follows Gaussian statistics, that is reflected by negative

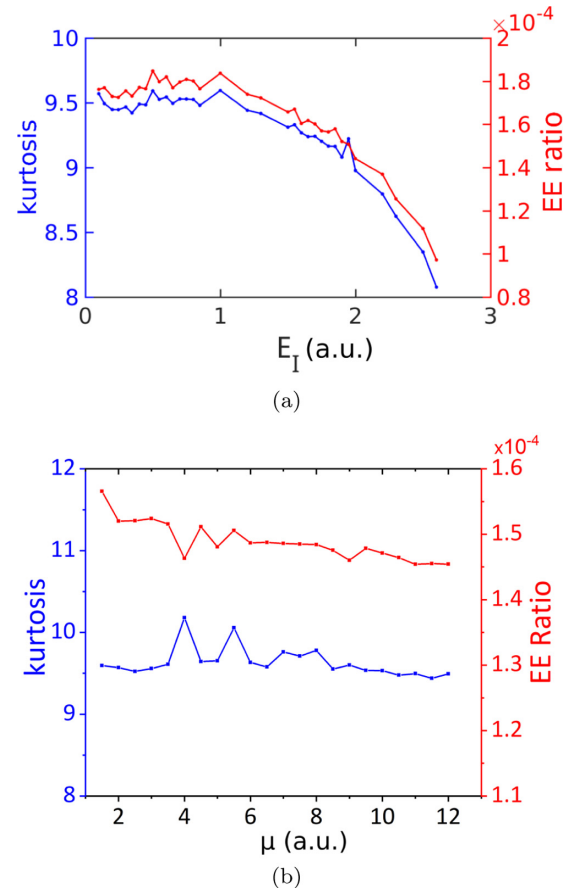


FIG. 2. Kurtosis  $\mathcal{K}$ , in blue (lower line), and extreme-event (EE) ratio, in red (upper line), of the total-intensity PDF for simulations with different (a) injection amplitudes  $E_I$  and (b) pump currents, respectively for  $\mu = 6$  (a) and  $E_I = 0.5$  (b). From these two indicators we can observe that extreme events are more likely to be observed for low values of  $E_I$ , while variations of pump current for fixed injection do not have a significant effect on extreme-event occurrence.

exponential behavior as  $\exp(-I_{\text{tot}}/\langle I_{\text{tot}} \rangle)/\langle I_{\text{tot}} \rangle$  for the PDF of the total intensity. Hence, any positive deviation from a negative exponential statistics has to be considered a signature of the presence of extreme events in the system. An indicator often used to characterize the extreme nature of the turbulent regime as a function of the injection is the kurtosis  $\mathcal{K}$ , which is the ratio of the fourth momentum about the mean of the data to the square of its variance. This statistical tool gives a measure of the tails of a distribution. Even though the kurtosis should not be interpreted as a measure of the heaviness of a distribution tail [31], a value of  $\mathcal{K}$  higher than 9 (which corresponds to a negative exponential) shows how much the tail of the considered distribution positively deviates from a negative exponential. In Fig. 2(a) we illustrate, with the blue lower line, the kurtosis of the total-intensity PDFs obtained from simulations for different values of optical injection and fixed pump current  $\mu = 6$ . Further, we display, with the red upper line, the ratio of extreme events occurring during each simulation according to a specific threshold of intensity. This threshold is defined in the literature (see, e.g., [2] and references therein) and corresponds to the mean of

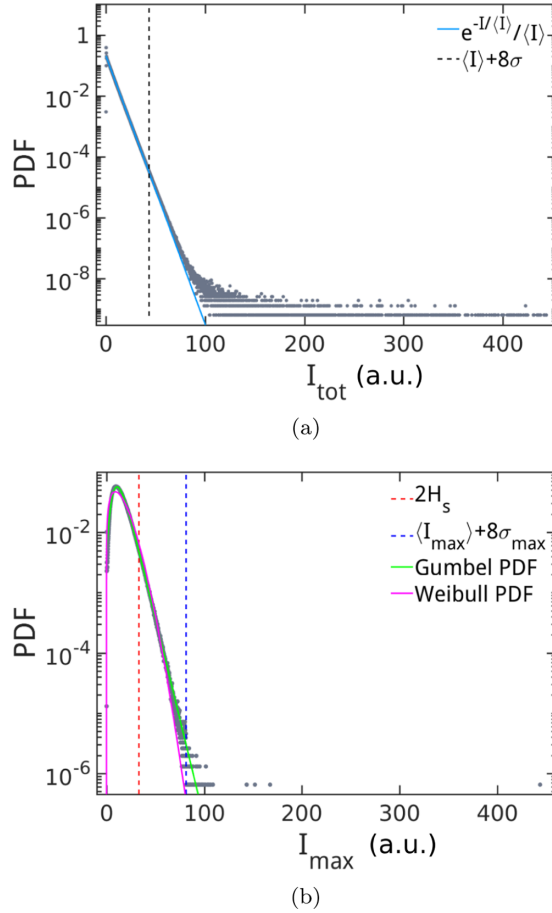


FIG. 3. Statistical analysis for a 250-ns-long simulation at  $\mu = 6$  and  $E_I = 0.1$ . (a) PDF of the total intensity, where we indicate (light-blue solid line) the negative exponential behavior which would be followed by the data in the case of Gaussian statistics. (b) PDF of the spatiotemporal maxima occurring during the simulation. The magenta (dark gray) and green (light gray) curves represent the Weibull and Gumbel PDFs from extreme value theory. The vertical black [in (a)], red [in (b), at lower intensity], and blue [in (b), at higher intensity] dashed lines indicate the extreme-event thresholds discussed in the text. Other parameters are  $\alpha = 4$ ,  $\theta = -2$ ,  $\sigma = 400$ , and  $d = 0.01$ .

the total intensity plus 8 times its standard deviation. Both indicators support the claim of extreme events in the system. Further, we can clearly observe that the biggest deviations from the negative exponential behavior of the data happen for low values of injection and correspond to a higher percentage of extreme events. The same is done in Fig. 2(b) for fixed injection amplitude ( $E_I = 0.5$ ) and variable pump current  $\mu$  (starting close to threshold), showing that the pump current does not appear to play a significant role in extreme-event occurrence.

Motivated by these results, we focus on a longer simulation at  $E_I = 0.1$ ,  $\mu = 6$ , and we report in Fig. 3(a) the total-intensity PDF for a 250-ns-long simulation ( $\mathcal{K} = 9.92$ ). We can observe the clear presence of a heavy tail in the data. Furthermore, we indicate with the vertical black dashed line the threshold for extreme events, defined as the average of the field intensity values plus 8 times their standard deviation.

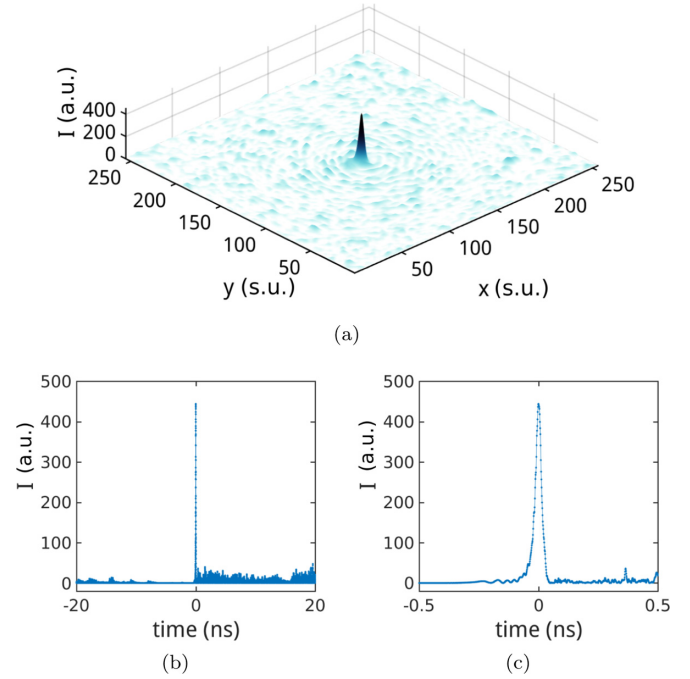


FIG. 4. (a) Three-dimensional intensity profile of an extreme event in the spatial transverse plane for the 250-ns-long simulation at  $\mu = 6$  and  $E_I = 0.1$  (s.u. stands for spatial units) and its temporal profile (b), zoomed in (c). The temporal axis in (b) and (c) and the space grid in (a) are centered on the extreme-event maximum.

In Fig. 3(b) we also illustrate the PDF of the spatiotemporal maxima occurring during the simulation. A spatiotemporal maximum is defined as a local spatial maximum in the transverse plane recorded in its temporal peak value [20]: statistics performed for data sets of spatiotemporal maxima allows us to identify any extreme event with a single data element, which is different from the previous analysis in which multiple data points correspond to a single event. With the vertical red dashed line (at lower intensities) we report another threshold for extreme events given by 2 times the significant wave height  $H_s$ , which is the mean of the highest third of the maximum data. Further, we report the more restrictive threshold (in blue, at higher intensities), which was already introduced in [20], given by the mean of the maximum data plus 8 times their standard deviation. By means of these two thresholds, this alternative statistical study further supports the claim of extreme events in the system. The magenta (dark gray) and green (light gray) curves represent the Weibull [ $ax^{k-1} \exp(-x^k)$  with  $x = I_{\max}/\lambda$  and  $a = k/\lambda$ ] and Gumbel ( $\exp\{-[z + \exp(-z)]\}/\beta$ , with  $z = (I_{\max} - \langle I_{\max} \rangle)/\beta + \gamma$  and  $\gamma$  being Euler's constant) PDFs as families of the generalized extreme-value distribution. The data are found to follow relatively well a Gumbel distribution but display a clear deviation for very high values of intensity. In general, in comparison with the system studied in [20] (a broad-area semiconductor laser with an intracavity saturable absorber and no external injection), we notice that the total-intensity statistics are more sensitive than the spatiotemporal maximum statistics to the presence of extreme events. In Fig. 4 we report the three-dimensional profile of an extreme event occurring during the simulation at

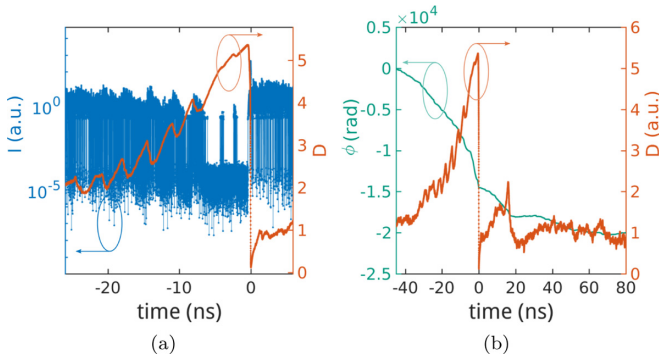


FIG. 5. Temporal trace in a single grid point for (a) laser intensity  $I$  (in logarithmic scale) and population  $D$  and (b) for phase  $\phi$  and population in the presence of the extreme event illustrated in Fig. 4.

$E_I = 0.1$ ,  $\mu = 6$  [Fig. 4(a)] as well as the (zoomed) temporal profile in the spatial grid point where the extreme event takes place [recentered at the occurrence time; Figs. 4(b) and 4(c)]. Given the periodic boundary conditions, we rearrange the spatial grid in Fig. 4(a) in order to visualize the extreme event at the center of the transverse plane. We can notice already in Fig. 4(b) that prior to an extreme event the laser intensity exhibits a couple of regular pulsations onto an almost zero background. In Fig. 5 we illustrate temporal profiles of the same maximum intensity point in logarithmic scale together with that of the population variable  $D$  [Fig. 5(a)] and the population at the location of the same maximum intensity point along with the (unwrapped) phase of the slowly varying envelope of the electric field [Fig. 5(b)].

The entire process of extreme-event occurrence can be observed in several stages: (i) 20 ns before the occurrence of an extreme event the population variable starts increasing and pulsating. (ii) This progressively leads to lower values of intensity, also through a pulsating behavior. (iii) When the population variable reaches its maximum and starts decreasing, the extreme event occurs. (iv) Finally,  $D$  rapidly drops to lower values ( $\approx 0-1$ ). From Fig. 5(b) we can also observe that, even before  $D$  starts increasing, the electric-field phase has started to monotonically decrease (instead of oscillating around zero, which is the usual behavior at other points of the grid). This dynamical description seems to be common to all the extreme events encountered for different values of pump current  $\mu$  and injection  $E_I$ .

In Fig. 6 we illustrate the trajectory of the same point in  $(I, \phi, D)$  phase space when approaching the extreme event. The blue solid line highlights the unstable focus point  $C$  [24] on the lower branch of the stationary curve in Fig. 1(a) for the chosen value of the injection amplitude ( $E_I = 0.1$ ).  $C$  has a specific value in phase, but given the large excursion in  $\phi$ , even marking such a value with a dot (with modulus  $2\pi$ ) visually results in a line along the phase axis for this scale. The trajectory evolves in time from green to yellow (in the direction of the arrows), and as the trajectory approaches the fixed point  $C$ , the phase starts to decrease, the amplitude of the electric field diminishes, and the population variable continues to increase. When the trajectory grows close enough to the fixed point, the repulsive nature of  $C$  pushes the system to spike in intensity, which is accompanied by a rapid decrease

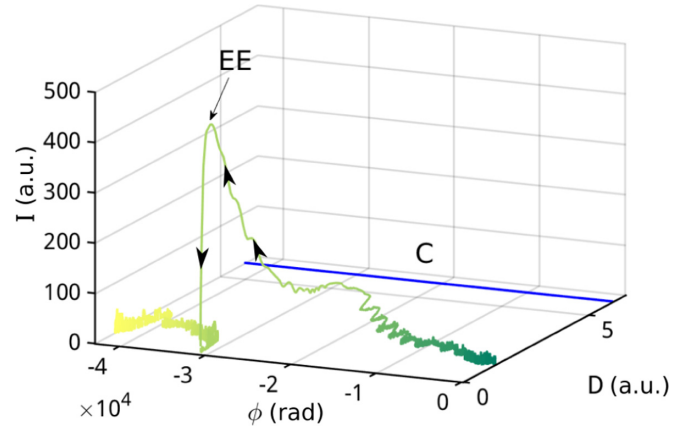


FIG. 6. Three-dimensional representation of the  $(I, \phi, D)$  phase space for the trajectory of a single grid point following the development of an extreme event. The trajectory evolves in time from green to yellow, as also illustrated by the arrows. The blue line (at high  $D$ ) highlights the unstable focus  $C$  of the HSS for the chosen value of injection ( $E_I = 0.1$ ).

in population. Finally, after the trajectory reaches its minimum in intensity and population,  $D$  starts to oscillate around 1. For longer times ( $t > 80$  ns), not illustrated in Fig. 6, the phase of the electric field starts to oscillate around a constant value, which would be zero if we took into account the  $2\pi$  modulus, which occurs at other points of the spatial grid lacking extreme events. Such a specific behavior for the phase variable allows us to anticipate the formation of extreme events up to 20 ns before their actual occurrence, which may potentially pave the way for their suppression through carefully thought out experimental techniques [32].

To further elucidate the role of the electric-field phase in the dynamics, its behavior in the transverse plane at the extreme-event occurrence time is shown in Fig. 7(a), where a red cross marks the location where the extreme event takes place. We can observe the presence of concentric structures around the red cross simultaneously with the occurrence of

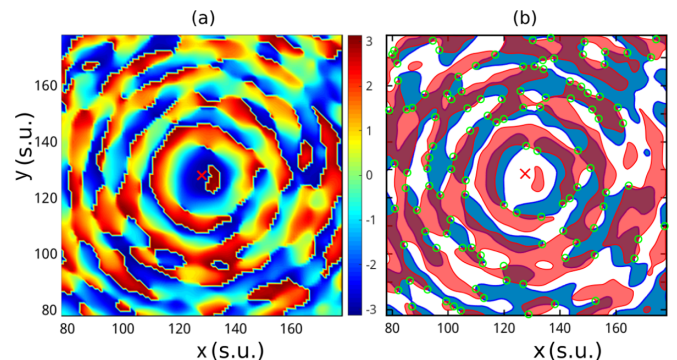


FIG. 7. (a) Phase and (b) contour plot for the real [blue (dark gray)] and imaginary [red (light gray)] parts of the electric field at the time of extreme-event occurrence in the spot highlighted by the red cross. In (b) the color-filled areas correspond to positive values for the respective variables; hence, the border of each area identifies a zero isoline. The crossings between blue and red isolines, highlighted by green circles, identify optical vortices.

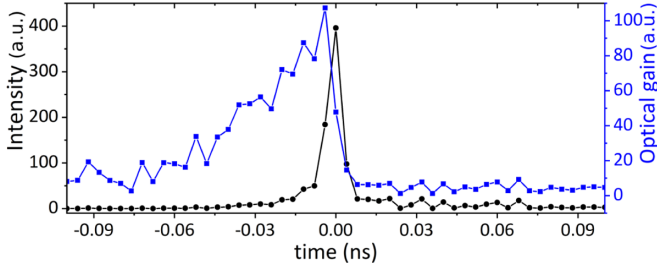


FIG. 8. Intensity (black line with circles) and optical gain (blue line with squares) values versus time at the point where the extreme event occurs (at time 0). The peak of the optical gain happens 4 ps before the extreme event. Control parameters are  $\mu = 8$  and  $E_l = 0.5$ .

ripples in the transverse profile of the laser intensity also evident in Fig. 4(a). It is important to observe that these ripples appear in the transverse plane long before the actual occurrence of the extreme event and are associated with the formation of vortices in the transverse plane around the extreme-event future location. To better justify this point in Fig. 7(b) we illustrate a contour plot for the real [blue (dark gray)] and imaginary [red (light gray)] parts of the electric field, where color-filled areas correspond to positive values for  $\text{Re}(E)$  and  $\text{Im}(E)$ , and the border of each area corresponds to a zero isoline for the respective variable. Each crossing between blue and red isolines in Fig. 7 corresponds to a zero for the laser intensity and gives rise to an optical vortex [33], further highlighted by green circles. Even if optical vortices (both positive and negative) occur all over the transverse plane, their specific configuration around extreme-event locations seems to participate in the formation of high-intensity structures.

#### IV. OPTICAL-GAIN ANALYSIS

Alongside the phase and population, a closer look into the optical-gain dynamics of the considered system can shed further light on the underlying mechanism of extreme-event formation and its prediction. The optical gain for the model in Eq. (1) can be defined as the absolute value of  $(1 - i\alpha)ED$  [26].

For a given set of control parameter values,  $\mu = 8$  and  $E_l = 0.5$ , we sketch in Fig. 8 the temporal trace of optical gain and intensity at the spatial location of an extreme event. Here, we observe that the optical gain reaches its maximum value 4 ps before the extreme-event occurrence.

To further this point, in Fig. 9 we show the trajectory in the subspace of intensity and optical gain. Here, the system trajectory is initially fluctuating around optical-gain values of 8 (a.u.) and usually remains below 20. Then, this fluctuating behavior changes, and the optical gain starts to grow beyond 70 about 22 ps before the occurrence of the extreme event, which increases the temporal range of a possible prediction window. Two clear peaks for the optical gain (marked by red asterisks in Fig. 9), one immediately before the event and another one after the gain starts its large excursion, can act as warnings for the upcoming extreme intensity peak. We can also observe that the extreme-event threshold based on the values of total intensity (vertical blue dashed line in Fig. 9)

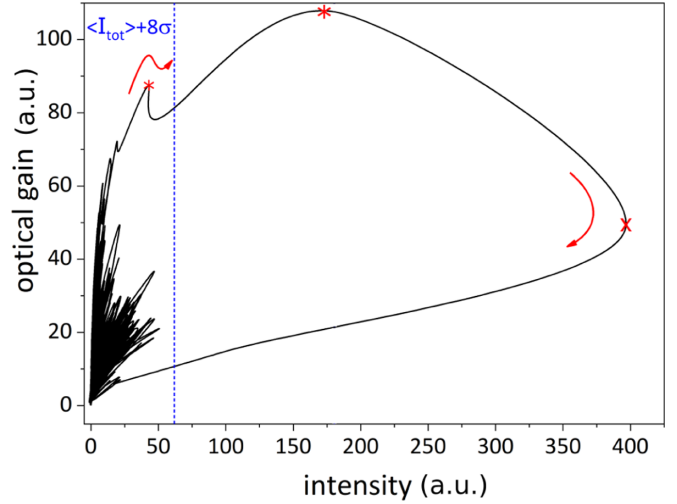


FIG. 9. Trajectory of the system in the (intensity, optical gain) subspace. When the fluctuating trend of the trajectory breaks, the relevant excursion leading to an extreme event begins. The arrows show the trajectory direction. The extreme event is marked by a red cross, while the optical-gain peaks are marked by red asterisks. The vertical dashed line corresponds to the extreme-event threshold as defined in Fig. 3(a). Parameters are the same as in Fig. 8.

occurs after the first optical-gain peak, which therefore seems more sensitive as an indicator of extreme-event behavior.

In order to summarize the evolution of the laser output in the proximity of an extreme event, we report in Fig. 10 the behavior of optical gain (top row), electric-field intensity (middle row), and phase (bottom row) in a time window of 24 ps with an extreme event occurring at  $t = 12$  ps (second column). Here, we can observe a peak in the optical gain occurring 12 ps before the formation of the extreme event in the electric-field intensity. Note also that, while the spatiotemporal maximum in optical gain occurs 12 ps before the event, if we were to consider the beginning of the optical-gain increase in the system trajectory, as illustrated in Fig. 9, this would allow for a larger prediction window. Vortices visible in the phase plots in Figs. 10(g) and 10(h) give rise to intensity ripples in Figs. 10(d) and 10(e), and this process represents a precursor of extreme-event occurrence in a time window of the order of tens of nanoseconds, as discussed in the previous section.

#### V. EXTREME EVENTS IN THE PRESENCE OF FINITE CIRCULAR PUMP

In all simulations we used periodic boundary conditions, which is required by the fast-Fourier-transform algorithm to solve the transverse Laplacian for the diffraction and diffusion terms. This assumption, which physically corresponds to an infinitely broad area for light emission in the transverse section of the laser, may give rise to unrealistic behaviors in simulations. Therefore, in order to confirm the results reported here, we replaced the flat pump current profile with the following function of the transverse plane coordinates, which simulates a finite circular pump profile with rapidly

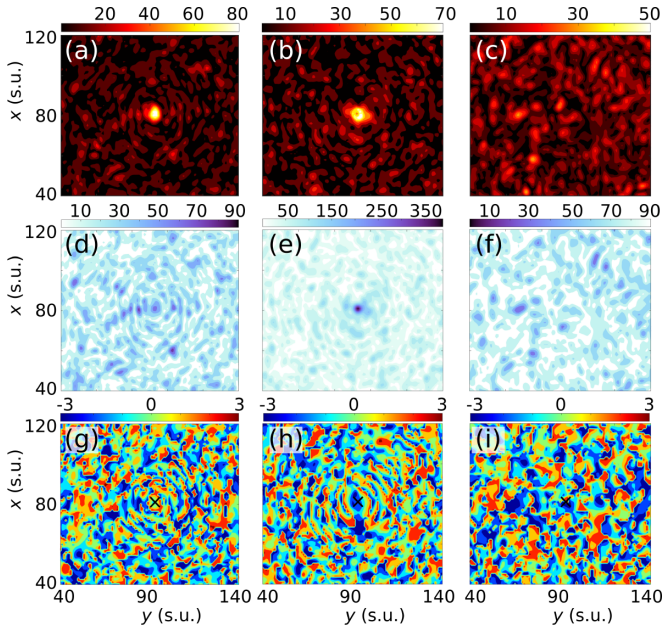


FIG. 10. Laser output variables in a zoom of the transverse plane at times 9.180 ns (first column), 9.192 ns (second column), and 9.204 ns (third column). Top row: optical gain (a.u.), reaching its maximum in (a). Middle row: electric-field intensity (a.u.), displaying an extreme event in (e). Bottom row: electric-field phase (rad), showing the presence of vortices around the location of the event (marked with a black cross). The optical-gain matrix shows a spatiotemporal maximum before the emission of the extreme event. Parameter values are the same as in Fig. 8.

decaying tails:

$$\mu(r) = \mu/2\{1 - \tanh[\rho(r - r_0)]\}, \quad (4)$$

where  $\rho$  and  $r_0$  regulate the size of the tail and flat part of the pump, respectively. In Fig. 11(a) we show the form of this circular flat-top pump profile along the  $x$  axis on a  $256 \times 256$  grid, together with that of the population  $D$  profile at the pump diameter during the simulation. In Fig. 11(b) we show instead the transverse snapshot of the intensity at the time of an extreme-event occurrence.

Performing the statistics of the total-intensity data in a simulation for  $\mu = 6$  and  $E_I = 0.5$  in the case of both infinite

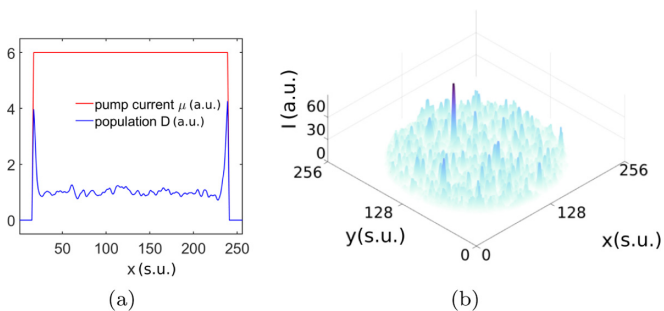
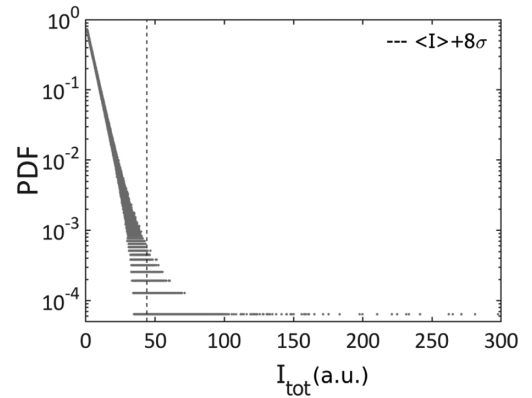
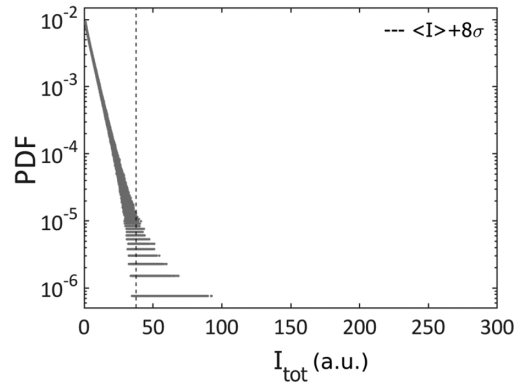


FIG. 11. (a) Profile of the finite-pump current of Eq. (4) (in red, with the flat-top shape) and population (in blue) at the pump diameter on the  $x$  axis. (b) Intensity snapshot at the time of extreme-event formation. Parameter values are  $\mu = 6$  and  $E_I = 0.5$ .



(a)



(b)

FIG. 12. Total-intensity statistics affected by finite pump: (a) PDF in the case of an infinite (flat) pump and (b) PDF for the circular flat-top pump. We can observe extreme events still occur in the presence of a finite-pump profile. Parameter values are  $\mu = 6$  and  $E_I = 0.5$  in both cases.

(flat) and finite circular pump profiles, we obtain the results illustrated in Fig. 12, where in the second case [Fig. 12(b)] the data outside the circular area of the pump were excluded. Here, we can observe that, while the presence of the finite pump affects the shape of the statistics, it does not inhibit the presence of extreme events. Note also that while both simulations were run for a total of 25 ns in order to compare these two PDFs beyond a qualitative level, the simulation in the finite-pump case should be extended so that the number of data points considered in the statistics is the same in both cases. However, as highlighted by Figs. 12(a) and 12(b), the deviation of the statistics from the defined threshold is still apparent, which makes all the arguments presented in this paper robust.

## VI. DISCUSSION

In contrast to the turbulent regime in VCSELs with a saturable absorber [20] (where extreme events were also observed), the kind of turbulence in the current system presents different features, namely, the active contribution of vortices in the formation of extreme events. This makes the system dynamically closer to similar setups with smaller spatial dimensionality, where phase chirality is responsible for both

the formation of phase solitons [23] and extreme events [24]. Further, we may also argue that, while in the case of Ref. [20] spatial effects have an important role in the overall system dynamics, which leads, for example, to the occurrence of soliton spatial drift instability [34], in the present case, our turbulent regime seems to develop more evidently in the temporal direction. This feature locks spatiotemporal structures in a specific spatial point, which is different from [20], in which structures would constantly move around in the transverse plane, and allows for a meaningful temporal profile at a single spatial point of the cavity as well as clearer identification of possible predictors for extreme events.

While the dynamical description illustrated in Fig. 6 is reminiscent of the results in [24] obtained for a semiconductor ring laser with optical injection and one spatial dimension along propagation, the main difference from the present case consists of the specific role played by the electric-field phase [35]. In particular, in [24] high-peak events arose from the interplay between positive and negative chiral charges, that is,  $\pm 2\pi$  phase rotations, which developed in the cavity due to the simultaneous presence of three fixed points: an unstable focus in the lower branch (point C in Fig. 6), a saddle on the negative-slope branch, and an unstable node on the upper branch of the HSS. In the present system, where the only fixed point is on the lower branch of the HSS, the electric-field phase in the location of the extreme event continuously decreases in time, giving rise to a very large number of negative charges, while optical vortices form around the event location contributing to the emergence of intensity ripples before its occurrence.

Optical vortices in the transverse plane were identified as a mechanism for the formation of extreme events in [15]

in a regime of vortex turbulence. In the present case, the dynamical description is more complex due to the slow population timescale and the semiconductor nature of the system. In particular, while in [15] the number of optical vortices was limited, in the present case we already noticed that vortices occur at all times and all over the transverse plane. Nevertheless, their specific configuration appears to still play a role in the formation of extreme events and is directly related to the formation of ripples in the laser intensity. Further similarities to the vortex turbulence of [15] remain to be investigated through a more in-depth regime characterization and will be addressed in future work.

## VII. CONCLUSIONS

We have observed the emergence of extreme events in a broad-area semiconductor laser with optical injection and justified their extreme nature through statistical analysis. Extreme events seem more frequent for high pump values and low values of optical injection. A detailed dynamical study on specific extreme events revealed a similar formation mechanism that involves a monotone temporal decrease in the electric-field phase, a pulsating increase of the population variable, and a maximum in the optical gain preceding the event, together with the emergence of optical vortices in the spatial transverse plane around the spot where the extreme event would take place. In particular, the process enhancing extreme events starts to be visible  $\gtrsim 20$  ns before the actual occurrence of the event. While a more systematic study will be necessary to further confirm these findings, the results obtained in this work allow us to suggest a potential predictor for extreme events in the system.

- 
- [1] D. R. Solli, C. Ropers, P. Koonath, and B. Jalali, Optical rogue waves, *Nature (London)* **450**, 1054 (2007).
  - [2] M. Onorato, S. Residori, U. Bortolozzo, A. Montina, and F. T. Arecchi, Rogue waves and their generating mechanisms in different physical contexts, *Phys. Rep.* **528**, 47 (2013).
  - [3] J. M. Dudley, F. Dias, M. Erkintalo, and G. Genty, Instabilities, breathers and rogue waves in optics, *Nat. Photonics* **8**, 755 (2014).
  - [4] N. Akhmediev *et al.*, Roadmap on optical rogue waves and extreme events, *J. Opt.* **18**, 063001 (2016).
  - [5] B. Kibler, J. Fatome, C. Finot, G. Millot, F. Dias, G. Genty, N. Akhmediev, and J. M. Dudley, The peregrine soliton in nonlinear fibre optics, *Nat. Phys.* **6**, 790 (2010).
  - [6] M. Erkintalo, K. Hammami, B. Kibler, C. Finot, N. Akhmediev, J. M. Dudley, and G. Genty, Higher-Order Modulation Instability in Nonlinear Fiber Optics, *Phys. Rev. Lett.* **107**, 253901 (2011).
  - [7] B. Kibler, J. Fatome, C. Finot, G. Millot, G. Genty, B. Wetzell, N. Akhmediev, F. Dias, and J. M. Dudley, Observation of Kuznetsov-Ma soliton dynamics in optical fibre, *Sci. Rep.* **2**, 463 (2012).
  - [8] *Nonlinear Guided Wave Optics*, edited by S. Wabnitz (IOP Publishing, Bristol, UK, 2017).
  - [9] S. Coulibaly, M. Taki, A. Bendahmane, G. Millot, B. Kibler, and M. G. Clerc, Turbulence-Induced Rogue Waves in Kerr Resonators, *Phys. Rev. X* **9**, 011054 (2019).
  - [10] C. Bonatto, M. Feyereisen, S. Barland, M. Giudici, C. Masoller, J. R. Rios Leite, and J. R. Tredicce, Deterministic Optical Rogue Waves, *Phys. Rev. Lett.* **107**, 053901 (2011).
  - [11] J. Zamora-Munt, B. Garbin, S. Barland, M. Giudici, J. R. Rios Leite, C. Masoller, and J. R. Tredicce, Rogue waves in optically injected lasers: Origin, predictability, and suppression, *Phys. Rev. A* **87**, 035802 (2013).
  - [12] J. M. Dudley, G. Genty, F. Dias, B. Kibler, and N. Akhmediev, Modulation instability, Akhmediev Breathers and continuous wave supercontinuum generation, *Opt. Express* **17**, 21497 (2009).
  - [13] M. Eslami, M. Khanmohammadi, R. Kheradmand, and G.-L. Oppo, Optical turbulence and transverse rogue waves in a cavity with triple-quantum-dot molecules, *Phys. Rev. A* **96**, 033836 (2017).
  - [14] M. Eslami, R. Kheradmand, D. McArthur, and G.-L. Oppo, Complex structures in media displaying electromagnetically induced transparency: Pattern multistability and competition, *Phys. Rev. A* **90**, 023840 (2014).
  - [15] C. J. Gibson, A. M. Yao, and G.-L. Oppo, Optical Rogue Waves in Vortex Turbulence, *Phys. Rev. Lett.* **116**, 043903 (2016).

- [16] S. Birkholz, C. Brée, A. Demircan, and G. Steinmeyer, Predictability of Rogue Events, *Phys. Rev. Lett.* **114**, 213901 (2015).
- [17] N. M. Alvarez, S. Borkar, and C. Masoller, Predictability of extreme intensity pulses in optically injected semiconductor lasers, *Eur. Phys. J.: Spec. Top.* **226**, 1971 (2017).
- [18] F. Selmi, S. Coulibaly, Z. Loghmari, I. Sagnes, G. Beaudoin, M. G. Clerc, and S. Barbay, Spatiotemporal Chaos Induces Extreme Events in an Extended Microcavity Laser, *Phys. Rev. Lett.* **116**, 013901 (2016).
- [19] S. Coulibaly, M. G. Clerc, F. Selmi, and S. Barbay, Extreme events following bifurcation to spatiotemporal chaos in a spatially extended microcavity laser, *Phys. Rev. A* **95**, 023816 (2017).
- [20] C. Rimoldi, S. Barland, F. Prati, and G. Tissoni, Spatiotemporal extreme events in a laser with a saturable absorber, *Phys. Rev. A* **95**, 023841 (2017).
- [21] K. Talouneh, C. Rimoldi, R. Kheradmand, G. Tissoni, and M. Eslami, Control of spatiotemporal rogue waves by harmonic pump modulation in a semiconductor laser with a saturable absorber, *Phys. Rev. A* **102**, 033508 (2020).
- [22] C. Bonazzola, A. Hnilo, M. Kovalsky, and J. R. Tredicce, Optical rogue waves in an all-solid-state laser with a saturable absorber: Importance of the spatial effects, *J. Opt.* **15**, 064004 (2013).
- [23] F. Gustave, C. Rimoldi, P. Walczak, L. Columbo, M. Brambilla, F. Prati, G. Tissoni, and S. Barland, Formation of phase soliton complexes in an optically injected semiconductor laser, *Eur. Phys. J. D* **71**, 154 (2017).
- [24] C. Rimoldi, F. Gustave, L. Columbo, M. Brambilla, S. Barland, F. Prati, and G. Tissoni, Abnormal chiral events in a semiconductor laser with coherent injection, *Opt. Express* **25**, 22017 (2017).
- [25] F. Gustave, L. Columbo, G. Tissoni, M. Brambilla, F. Prati, B. Kelleher, B. Tykalewicz, and S. Barland, Dissipative Phase Solitons in Semiconductor Lasers, *Phys. Rev. Lett.* **115**, 043902 (2015).
- [26] X. Hachair, F. Pedaci, E. Caboche, S. Barland, M. Giudici, J. R. Tredicce, F. Prati, G. Tissoni, R. Kheradmand, L. A. Lugiato, I. Protzenko, and M. Brambilla, Cavity solitons in a driven VCSEL above threshold, *IEEE J. Sel. Top. Quantum Electron.* **12**, 339 (2006).
- [27] S. R. Anbardan, C. Rimoldi, R. Kheradmand, G. Tissoni, and F. Prati, Exponentially decaying interaction potential of cavity solitons, *Phys. Rev. E* **97**, 032208 (2018).
- [28] S. V. Fedorov, A. G. Vladimirov, G. V. Khodova, and N. N. Rosanov, Effect of frequency detunings and finite relaxation rates on laser localized structures, *Phys. Rev. E* **61**, 5814 (2000).
- [29] M. Eslami, R. Kheradmand, and K. M. Aghdami, Complex behavior of vertical cavity surface emitting lasers with optical injection, *Phys. Scr.* **2013**, 014038 (2013).
- [30] M. Eslami and G.-L. Oppo, Nonlinear dynamics of triple quantum dot molecules in a cavity: Multi-stability of three types of cavity solitons, *Eur. Phys. J. D* **75**, 125 (2021).
- [31] K. P. Balanda and H. L. Macgillivray, Kurtosis: A critical review, *Am. Stat.* **42**, 111 (1988).
- [32] H. L. D. de S. Cavalcante, M. Oriá, D. Sornette, E. Ott, and D. J. Gauthier, Predictability and Suppression of Extreme Events in a Chaotic System, *Phys. Rev. Lett.* **111**, 198701 (2013).
- [33] P. Couillet, L. Gil, and J. Lega, Defect-Mediated Turbulence, *Phys. Rev. Lett.* **62**, 1619 (1989).
- [34] F. Prati, G. Tissoni, L. A. Lugiato, K. M. Aghdami, and M. Brambilla, Spontaneously moving solitons in a cavity soliton laser with circular section, *Eur. Phys. J. D* **59**, 73 (2010).
- [35] S. Barland, M. Brambilla, L. Columbo, B. Garbin, C. J. Gibson, M. Giudici, F. Gustave, C. Masoller, G. L. Oppo, F. Prati, C. Rimoldi, J. R. Rios, J. R. Tredicce, G. Tissoni, P. Walczak, A. M. Yao, and J. Zamora-Munt, Extreme events in forced oscillatory media in zero, one and two dimensions, in *Nonlinear Guided Wave Optics* (IOP Publishing, Bristol, UK, 2017), Chap. 1, pp. 1–28.